



1 Modelling of street-scale pollutant dispersion by coupled simulation of
2 chemical reaction, aerosol dynamics, and CFD

3 Chao Lin ^{a,*}, Yunyi Wang ^{b,*}, Ryoza Ooka ^c, Cédric Flageul ^d, Youngseob Kim ^b,
4 Hideki Kikumoto ^c, Zhizhao Wang ^b, Karine Sartelet ^b

5 ^a Graduate School of Engineering, The University of Tokyo, 4-6-1 Komaba, Meguro-ku,
6 Tokyo 153-8505, Japan

7 ^b CEREAs, École des Ponts ParisTech, EDF R&D, 77 455 Marne la Vallée, France

8 ^c Institute of Industrial Science, The University of Tokyo, 4-6-1 Komaba, Meguro-ku,
9 Tokyo 153-8505, Japan

10 ^d Curiosity Group, Pprime Institute, Université de Poitiers, CNRS, ISAE-ENSMA,
11 Chasseneuil, France

12 * Corresponding author, c-lin415@iis.u-tokyo.ac.jp

13 ★ These authors contributed equally to this work.

14

15 ABSTRACT

16 In the urban environment, gas such as nitrogen dioxide NO₂, and particles impose adverse
17 impacts on pedestrians' health. The conventional computational fluid dynamics (CFD)
18 methods that regard pollutant as passive scalar cannot reproduce the formation of
19 secondary pollutants, such as NO₂ and secondary inorganic and organic aerosols, leading
20 to uncertain prediction. In this study, SSH-Aerosol, a modular box model that simulates
21 the evolution of gas, primary and secondary aerosols, is coupled with the CFD software
22 OpenFOAM and Code_Saturne. The transient dispersion of pollutants emitted from
23 traffic in a street canyon is simulated using unsteady Reynolds-averaged Navier–Stokes
24 equations (RANS) model.

25 The simulated concentrations of NO₂, PM₁₀ and black carbon are compared with field
26 measurements on a street of Greater Paris. The simulated NO₂ and PM₁₀ concentrations
27 based on the coupled model achieved better agreement with measurement data than the
28 conventional CFD simulation. Meanwhile, the black carbon concentration is
29 underestimated, probably partly because of the underestimation of non-exhaust emissions
30 (tyre and road wear).

31 Vehicles are considered the main source of ammonia (NH₃) in urban environments, which
32 may condense with nitric acid (HNO₃) to form ammonium nitrate. In the reference
33 simulation with NH₃ traffic emissions accounting for 1-2% of NO_x emissions, aerosol
34 dynamics leads to an ammonium nitrate increase of 46% on average over a 12-hour
35 simulation period (5 a.m. to 5 p.m.) compared to the conventional CFD simulation.
36 Furthermore, an increase in NH₃ traffic emissions (to 10% and 20% of NO_x emissions)



37 may leads to a large increase in ammonium nitrate (35% and 55%) compared to the
38 reference simulation.

39 In addition, aerosol dynamics leads to a 52% increase in 12-hour time-averaged organic
40 matter concentrations compared to the conventional CFD simulation, because of the
41 condensation of anthropogenic compounds from precursor-gas emissions and of
42 background biogenic precursor-gases on the enhance inorganic concentrations.

43

44 Keywords

45 Pollutant dispersion, Street canyon, Aerosol dynamics, CFD, PM₁₀, Secondary aerosols

46

47 **1. Introduction**

48 Traffic-related pollutants can impose adverse effects on pedestrians' health in the urban
49 environment (Jones et al., 2008; Anenberg et al., 2017). Especially, particulate matter
50 (PM) is strongly associated with increased cardiovascular diseases (Du et al., 2016).
51 Therefore, investigating the dispersion of PM and the corresponding precursor gas is of
52 great significance to evaluate the environmental impact and devise suitable
53 countermeasures (Kumar et al., 2008).

54 With the development of numerical simulations, computational fluid dynamics (CFD) has
55 been widely used for near-field dispersion prediction (Tominaga and Stathopoulos, 2013).
56 The pollutant dispersion patterns in complex geometric and non-uniform building
57 configurations can be well predicted using CFD simulations (Blocken et al., 2013).
58 Pollutant dispersion, deposition and transformation (chemical reactions and aerosol
59 dynamics) have primary roles in near-field prediction models. However, most CFD-based
60 studies assume that the time scale of transport at the street scale (~ 100 m) is relatively
61 shorter than the time scale of deposition and transformation; therefore, they frequently
62 regard pollutants as inert matter. Meanwhile, the recirculation flows which commonly
63 exist in street canyons lead to low-ventilation zones and may provide sufficient time for
64 transformation (Lo and Ngan, 2017; Zhang et al., 2020).

65 In addition, when PM is transported as a passive scalar, the distribution of the total
66 concentration can be simulated, however, information on the particle size distribution and
67 chemical composition is unclear. Understanding the size distribution is important for
68 evaluating the health hazards because large particles are deposited in the mouth and upper
69 airways, whereas smaller particles deposit deeper in the lungs and can even reach the
70 alveolar region of the lungs (Sung et al., 2007). In addition, as particles of different
71 chemical compositions are related to different sources and/or precursor gases, gaining
72 knowledge of their composition may help devise countermeasures to limit their



73 concentrations (Kim, 2019).

74 To simulate pollutant concentrations considering both transport and transformation, many
75 studies have coupled air-quality models with gas-phase chemistry and aerosol modules
76 and achieved chemical transport from a regional scale (~100 km) (Sartelet et al., 2007) to
77 a street scale (Lugon et al., 2021b). However, few models can simultaneously represent
78 detailed particle dispersion in a complicated urban flow field considering secondary
79 aerosol formation.

80 For the recent development and application of CFD-chemistry coupling model, Kurppa
81 et al. (2019) implemented a sectional aerosol module into large eddy simulation (LES),
82 and conducted a particle dispersion simulation on a neighborhood scale. Gao et al. (2022)
83 employed the same model to examine the dispersion of cooking-generated aerosols in an
84 urban street canyon. In both studies, the effect of particle dynamics on aerosol number
85 concentration was well reproduced. However, the simulated chemical composition was
86 not detailed. In addition, the chemical reactions of the precursor gas were not considered.
87 Kim et al. (2019) coupled unsteady Reynolds-averaged Navier-Stokes (RANS) model
88 with gas chemistry and aerosol modules and conducted simulations of PM₁ in a street
89 canyon under summer and winter conditions. The diurnal variations, spatial distribution
90 and chemical composition of pollutants in the street canyon were investigated. However,
91 the size distribution of particles and the secondary organic aerosol (SOA) chemistry were
92 not considered.

93 Therefore, to achieve a more comprehensive simulation of PM and related precursor gas,
94 this study coupled two open-source CFD softwares: OpenFOAM (OpenFOAM, 2020)
95 and Code_Saturne (Archambeau et al., 2004), with gas-phase chemistry and aerosol
96 module SSH-Aerosol (Sartelet et al., 2020). Simulations of the PM concentrations in a
97 two-dimensional street canyon are conducted. The coupled model is validated by
98 comparison to field measurements. The size distributions and chemical compositions of
99 particles from the models with and without secondary aerosol formation are compared.

100 Vehicles are considered the main ammonia (NH₃) source in urban environments (Sun et
101 al., 2017). Reactive nitrogen emissions from many new model year vehicles are now
102 dominated by NH₃ (Bishop and Stedman, 2015). Since the formation of ammonium
103 nitrate is often limited by HNO₃ rather than NH₃ in urban areas (NH₃-limited), increasing
104 NH₃ may lead to increased ammonium nitrate production and PM concentration in urban
105 streets (Lugon et al., 2021b). However, NH₃ emissions from passenger cars are usually
106 not regulated (Suarez-Bertoa and Astorga, 2018). Therefore, to provide evidence in
107 making policies for NH₃ emission regulation, it is important to investigate the local
108 influence of NH₃ emissions on PM increase. As an illustration, cases considering large



109 NH₃ emissions are considered and the related PM increase is investigated.
110 The remainder of this paper is organized as follows. The coupling of the aerosol model
111 and CFD is introduced in Section 2. The computational details are presented in Section 3.
112 In Section 4, the simulated pollutant concentrations are compared with field
113 measurements, followed by evaluations of the influence of the grid, coupling method and
114 time step. In Section 5, spatial and temporal variations in the concentrations are analyzed.
115 The chemical compositions and size distributions of the particles between the coupled
116 model and the model that does not consider gas chemistry or aerosol dynamics are
117 compared. In addition, the effect of NH₃ traffic emissions on particle concentrations is
118 discussed. Finally, the conclusions and perspectives are presented in Section 6.

119

120 **2. Model description**

121 OpenFOAM v2012 and Code_Saturne 6.2 were used to solve the governing equations of
122 the flow field and transport equations of gas and particle mass fractions. The unsteady
123 RANS model was used for the transient simulations with both CFD codes. In OpenFOAM,
124 the RNG k - ϵ model (Yakhot et al., 1992) is deployed for turbulence closure. All transport
125 equations are discretized using the total variation diminishing (TVD) scheme (Harten,
126 1984; Yee, 1987), which combines the first-order upwind difference scheme and the
127 second-order central difference scheme. The PIMPLE algorithm, a merged PISO–
128 SIMPLE algorithm in the OpenFOAM toolkit, was used for pressure–velocity coupling.
129 In Code_Saturne, turbulence was solved using the k - ϵ turbulence model (linear
130 production) (Guimet and Laurence, 2002). The time and space discretizations of velocity,
131 pressure and other scalars in all transport equations are realized through a centred scheme
132 and a fractional step scheme (Archambeau et al., 2004). For both CFD software, the dry
133 deposition schemes for gas and particle are added to the transport equations using volume
134 sink terms based on Zhang et al. (2003) and Zhang et al. (2001), respectively. The details
135 of the implementation are provided in Appendix A.

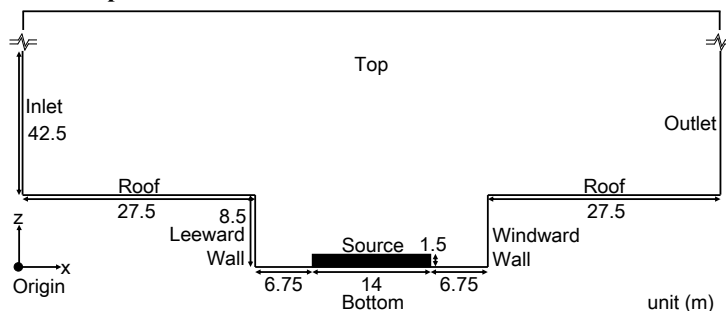
136 SSH-Aerosol (Sartelet et al., 2020) is a modular box model that simulates the evolution
137 of not only gas concentrations but also the mass and number concentrations of primary
138 and secondary particles. In SSH-Aerosol 112 gas species and 40 particle species are
139 considered. The particle compounds are dust, black carbon, inorganics (sodium, sulphate,
140 ammonium, nitrate and chloride), primary organic aerosol (POA) and secondary organic
141 aerosol (SOA). Three main processes involved in aerosol dynamics (coagulation,
142 condensation /evaporation and nucleation) are included. The particle size distribution is
143 modelled using a sectional size distribution. In this study, nucleation was not considered
144 and six particle size sections were employed with bound diameters of 0.01, 0.04, 0.16,



145 0.4, 1.0, 2.5 and 10 μm .
146 The coupling between CFD and SSH-aerosol was achieved by using the application
147 program interface (API) of SSH-aerosol. The gas and particle concentrations were
148 initialized in CFD and are transported in the domain for each time step. For each grid
149 volume cell, these transported concentrations, as well as meteorological parameters, such
150 as temperature and humidity, are then sent to SSH-aerosol to advance one time step of
151 gaseous chemistry and aerosol dynamics. Once the SSH-aerosol calculation was
152 completed, the concentrations were sent back to the CFD for the next time step. The
153 influence of different operator splitting algorithms is discussed in Section 4.4.

154

155 3. Simulation setup



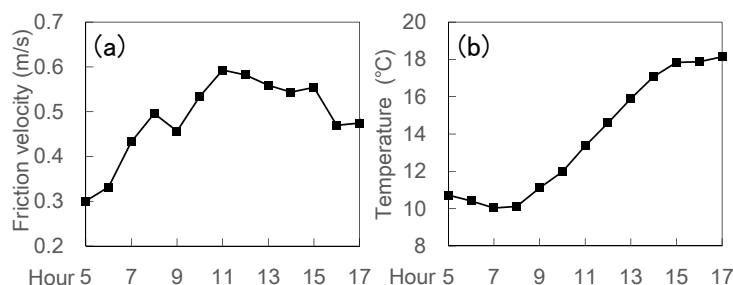
156

157 Fig. 1 Simulation domain of street canyon

158

159 The simulation was set up to model a street in Greater Paris (Boulevard Alsace-Lorraine),
160 where field measurements were conducted from April 6 to June 15, 2014. The
161 concentrations of nitrogen dioxide (NO_2), particles with diameters less than 10 μm (PM_{10}),
162 and black carbon were measured as described in Kim et al. (2018). Fig. 1 shows the
163 simulation domain. The 2-D street canyon is 27.5 m in width (W) and 8.5 m in height
164 (H). The domain height was 6 H . The street canyon was discretized into uniform grids in
165 x - and z - directions. An analysis of the grid sensitivity is described in Section 4.3.

166 Simulations were conducted from 4:30 a.m. to 5 p.m. on April 30, 2014 at local time
167 (GMT+2). This period was selected because the wind direction was almost perpendicular
168 to the street canyon during that day, allowing for a 2D simulation setting. The first 30
169 minutes of the simulation corresponded to model spin-up, and the simulation lasted 12
170 hours. A sensitivity analysis of numerical aspects, such as the splitting method between
171 transport and chemistry and the time step, is described in Section 4.4.



172

173 Fig. 2 Time variations of hourly friction velocity and temperature for inflow

174

175 Meteorological conditions (Fig. 2) including time-varying friction velocity and
 176 temperature were obtained from the simulation described in Sartelet et al. (2018) using
 177 the Weather Research and Forecasting (WRF) model. The lowest and highest friction
 178 velocities occurred approximately at 5 a.m. and 11 a.m., respectively. The lowest and
 179 highest temperatures occurred around 8 a.m. and 5 p.m. For the inflow, the wind direction
 180 was perpendicular to the street canyon. The friction velocity u_* is used to prescribe the
 181 vertical profiles of the streamwise velocity U , turbulent kinetic energy k and turbulent
 182 dissipation rate ε as follows

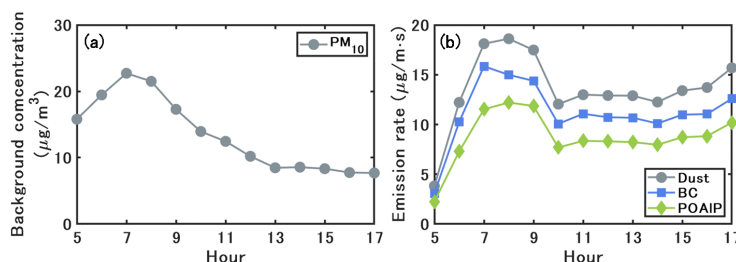
$$U(z) = \frac{u_*}{\kappa} \ln\left(\frac{z-H}{z_0}\right) \quad (1)$$

$$k(z) = \frac{u_*^2}{\sqrt{C_\mu}} \quad (2)$$

$$\varepsilon(z) = \frac{u_*^3}{\kappa(z-H)} \quad (3)$$

183 where κ is the von Kármán constant and C_μ is the model constant (=0.09) in the k- ε
 184 model. The roughness length z_0 is set to 1 m for the inlet (Belcher, 2005) and 0.1 m for
 185 the wall and bottom (Lo and Ngan, 2015).

186



187

188 Fig. 3 Time variations of PM₁₀ background concentration (left panel) and emission rates



189 of dust, BC and organics (POAIP) (right panel).

190

191 Fig. 3 shows the time variations of the PM₁₀ background concentrations and emission
192 rates for the emitted compounds of PM₁₀. The background concentrations of the gas and
193 particles are obtained from the regional-scale simulations of Sartelet et al. (2018). The
194 hourly background concentrations were linearly interpolated into seconds and prescribed
195 at the inflow and top. The traffic emission source is assumed to be approximately 14 m
196 in width and 1.5 m in height, and it is set in the middle of the bottom of the canyon (Fig.
197 1). As detailed in Kim et al. (2022), emissions are estimated from the fleet composition
198 and the number of vehicles in the street using COPERT's emission factors (COMputer
199 Program to calculate Emissions from Road Transport, version 2019, EMEP/EEA, 2019).
200 After the speciation of NO_x, Volatile Organic Compounds (VOC), PM_{2.5} and PM₁₀ into
201 model species, emissions were set for 16 gaseous model species and three particle model
202 species: dust and unspecified matter (Dust), black carbon (BC) and primary organic
203 aerosol of low volatility (POAIP).

204 For the boundary conditions of the OpenFOAM, the pressure and the gradients of all other
205 variables were set to zero at the outlet. For the walls, we used the wall functions of ε and
206 turbulent kinematic viscosity ν_t for atmospheric boundary layer modelling in
207 OpenFOAM toolkit (OpenFOAM, 2020) based on Parente et al. (2011). The gradients of
208 turbulent kinetic energy k , concentration, and temperature were set to zero. In
209 Code_Saturne, a two-scales logarithmic friction velocity wall function was used for
210 solving the fluid velocity near wall cell and a three layers wall function is used for
211 computing other transported scalar profiles such as temperature near the wall (Arpaci and
212 Larsen, 1984).

213 The turbulent Schmidt number Sc_t in the concentration transport equations, which is the
214 ratio of the turbulent diffusivity to the concentration and turbulent kinematic viscosity, is
215 important in turbulent diffusion modeling. The value of Sc_t is considered between 0.2
216 and 1.3, depending on the flow properties and geometries (Tominaga and Stathopoulos,
217 2007). For urban environments with a compact layout, a small $Sc_t = 0.4$ is found to
218 show better agreement with wind tunnel experiment data (Di Sabatino et al., 2007).
219 Therefore, a value of 0.4 is adopted in the current study.

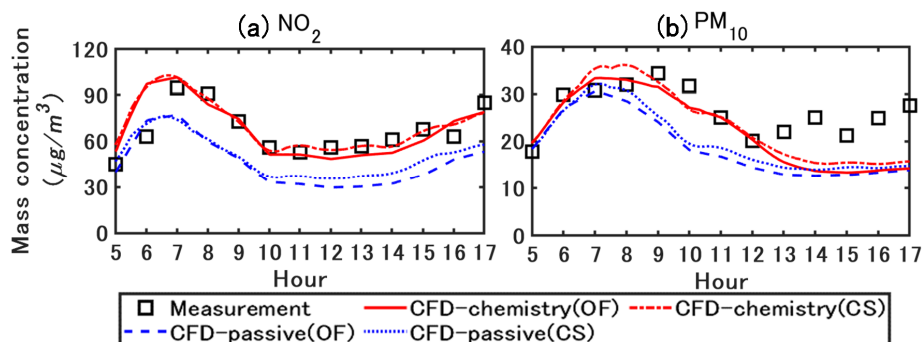
220

221 **4. Model evaluation**

222 *4.1. Validation with field measurements and comparison of simulated concentrations with*



223 the two CFD software



224

225 Fig. 4 Measured and simulated NO_2 and PM_{10} concentrations. The values are spatially
226 averaged in the street canyon ($27.5 \leq x \leq 55, 0 \leq z \leq 8.5$ m). CFD-passive and CFD-
227 chemistry denote the CFD simulation without and with chemistry coupling. OF and CS
228 denote the simulated concentrations based on OpenFOAM and Code_Saturne. All
229 concentrations are represented in local time (GMT+2).

230

231 Fig. 4 compares the simulated concentrations with those obtained from the field
232 measurements. In this section, the results and discussion are based on the spatially-
233 averaged values in the street canyon ($27.5 \leq x \leq 55, 0 \leq z \leq 8.5$ m). CFD-passive and
234 CFD-chemistry denote the CFD simulation without and with chemistry coupling. OF and
235 CS denote simulated concentrations based on OpenFOAM and Code_Saturne. The
236 operator splitting order and time step for OF and CS are the Strang method with 0.5 s and
237 the first order method with 0.25 s, as detailed in Section 4.4.

238 For NO_2 , the peak concentration in the field measurement occurred approximately at 7
239 a.m. owing to the morning traffic. In the CFD-passive simulations, the lack of chemical
240 reactions lead to an underestimation of NO_2 , while the concentrations simulated with
241 CFD-chemistry agree well with the measurements. For PM_{10} , the concentrations
242 simulated with CFD-chemistry also show better agreement with the measurements than
243 CFD-passive. The primary reason is that CFD-chemistry can reproduce the condensation
244 of inorganic and organic matters from the gas phase to the particle phase, which will be
245 further explained in the following sections. The simulation results based on OF and CS
246 show small differences, and detailed comparisons are presented in Fig. 6.

247 Validation metrics (Chang and Hanna, 2004) were used to quantify the overall accuracy
248 of the CFD simulated concentrations based on OF, compared with the measured values
249 (Ferrero et al., 2019; Trini Castelli et al., 2018). The following metrics were used:
250 fractional bias (FB), geometric mean bias (MG) and normalized mean square error



251 (NMSE). These metrics are defined as follows:

$$FB = \frac{\overline{Obs} - \overline{CFD}}{0.5(\overline{Obs} + \overline{CFD})} \quad (4)$$

$$MG = \exp(\ln \overline{Obs} - \ln \overline{CFD}) \quad (5)$$

$$NMSE = \frac{(\overline{Obs}_i - \overline{CFD}_i)^2}{\overline{Obs} \times \overline{CFD}} \quad (6)$$

252 where Obs_i and CFD_i are the measured and CFD simulated concentrations for the
253 compound/species i , respectively. The overbar represents the mean value of the entire
254 dataset. The ideal values are 1 for MG, and 0 for FB and NMSE. Previous research has
255 suggested that $|FB| < 0.3$, $0.7 < MG < 1.3$ and $NMSE < 4$ are acceptable for
256 simulated concentrations (Hanna et al., 2004).

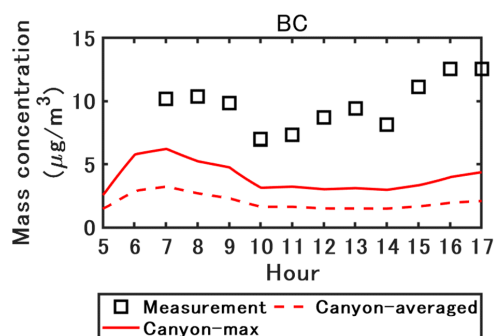
257 Table 1 shows the statistical indicators for spatially averaged concentrations of NO_2 and
258 PM_{10} in the street canyon from 5 a.m. to 5 p.m. For NO_2 and PM_{10} , the mean and 90%
259 percentile concentrations simulated with CFD-chemistry are closer to the measurements
260 than those simulated with CFD-passive. In addition, the FB, MG and NMSE values of
261 CFD-chemistry are closer to the ideal values than those of CFD-passive.

262

263 Table 1 Statistical indicators for NO_2 and PM_{10} in the street canyon from 5 a.m. to 5p.m.
264 The concentrations are simulated with OpenFOAM.

	Concentration ($\mu\text{g}/\text{m}^3$)		Validation metrics		
	Mean	Percentile 90%	FB	MG	NMSE
<u>NO_2</u>					
Measurement	66.6	91.8	/	/	/
CFD-chemistry	67.3	97.3	-0.01	1.00	1E-4
CFD-passive	45.9	73.7	0.36	1.50	0.14
<u>PM_{10}</u>					
Measurement	26.4	32.5	/	/	/
CFD-chemistry	22.3	33.1	0.17	1.23	0.03
CFD-passive	18.8	28.9	0.34	1.45	0.13

265

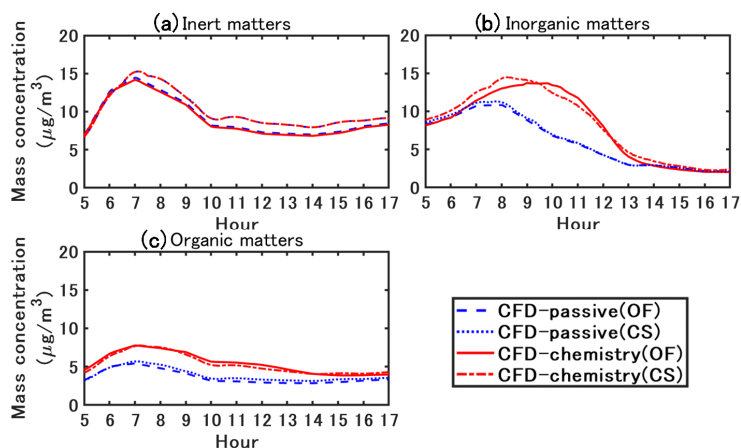


266

267 Fig. 5 Measured and simulated black carbon concentrations with OpenFOAM. The
268 canyon-averaged and maximum concentrations in the street canyon are represented by
269 the plain line and the dashed line respectively ($27.5 \leq x \leq 55, 0 \leq z \leq 8.5$ m).

270

271 The black carbon (BC) concentration simulated with OF was compared with the
272 measurements in Fig. 5. Because BC is considered an inert matter, considering chemistry
273 does not influence the mass concentration. Therefore, the concentrations simulated with
274 CFD-passive and CFD-chemistry show little difference; only the concentration simulated
275 with CFD-chemistry is shown here. The BC concentrations were underestimated by a
276 factor of approximately 5. Even the maximum concentrations in the street canyon largely
277 underestimate the measurements. One of the causes of this underestimation may be the
278 underestimation of the non-exhaust tyre emission factors in the COPERT emission factors
279 used here (Lugon et al., 2021a).



280

281 Fig. 6 Simulated particle concentrations with OpenFOAM (OF) and Code_Saturne (CS).
282 CFD-passive and CFD-chemistry denote the CFD simulation without and with chemistry



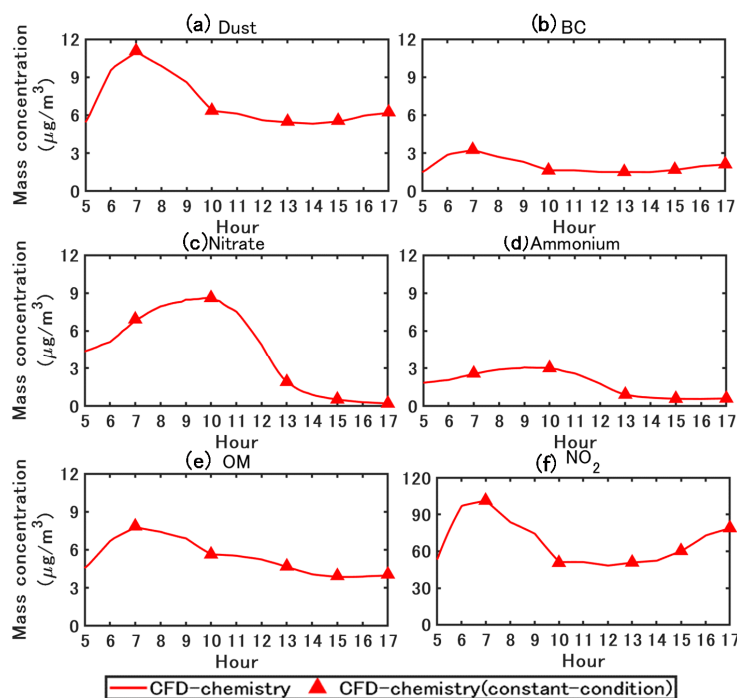
283 coupling.

284

285 The particle concentrations simulated with OF and CS are compared in Fig. 6. The
286 evolutions of the concentrations simulated by OF and CS were similar. Higher PM₁₀
287 concentrations were simulated by CS around 8 a.m. during the traffic peak and in the
288 afternoon, mostly because of the higher concentrations of emitted inert compounds, such
289 as black carbon and dust. Differences in the turbulence scheme may explain these
290 variations. Meanwhile, the difference between CFD-passive and CFD-chemistry for the
291 inorganic and organic matters was in accordance with OF and CS, showing the robustness
292 of the coupling method between CFD and SSH-aerosol by API. For simplicity, only the
293 simulated concentration based on OF is presented and discussed in the following sections.

294

295 4.2. Transient-condition method and constant-condition method



296

297 Fig. 7 Simulated PM₁₀ and NO₂ concentrations with the transient-condition and constant-
298 condition methods. The concentrations are spatially averaged in the street canyon.

299

300 Because time-varying concentrations are expensive to compute in terms of computational
301 time, conducting CFD simulations with fixed boundary conditions and emission rates at

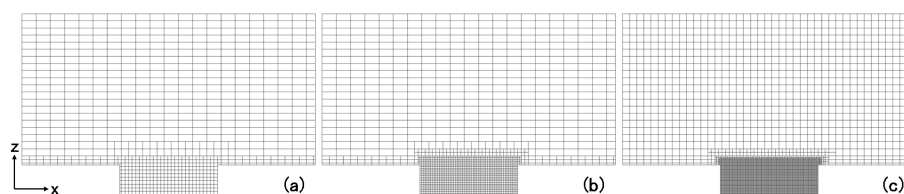


302 specific time points is considered a practical method for evaluating street-level pollutant
303 concentrations (Wu et al., 2021; Zhang et al., 2020). The transport (advection and
304 diffusion) and chemical processes reached equilibrium, and the simulated concentrations
305 reached quasi-stable values. These values are often regarded as time-averaged
306 concentrations. This method is called the constant-condition method (CCM) in this study,
307 in contrast to the transient-condition method (TCM). However, the simulation accuracy
308 of CCM has not been validated in simulations that consider both gas chemistry and
309 particle dynamics. Therefore, validation was conducted using boundary conditions and
310 emission rates at five time points (7 a.m., 10 a.m., 1 p.m., 3 p.m. and 5 p.m.). Other
311 simulation conditions, including the grid, coupling method, and time step, are the same
312 as the transient-condition simulation.

313 In Fig. 7, for PM_{10} and NO_2 , the concentrations simulated with CCM (red triangles) were
314 similar to those simulated with TCM. In addition, depending on the background
315 concentration and emission conditions, the simulation time required for CCM to reach
316 dynamic equilibrium is less than 1000 time steps (approximately 500 s). Therefore, CCM
317 can be utilized for parameter studies. The sensitivity analysis of the grid, coupling method
318 and time step in Section 4.3 and 4.4 is based on CCM. However, it should be noted that
319 CCM cannot replace TCM when simulating long periods because the mass concentration
320 may not change linearly between the selected time points. The simulated concentrations
321 in Section 5 were based on TCM.

322

323 4.3. Grid sensitivity



324

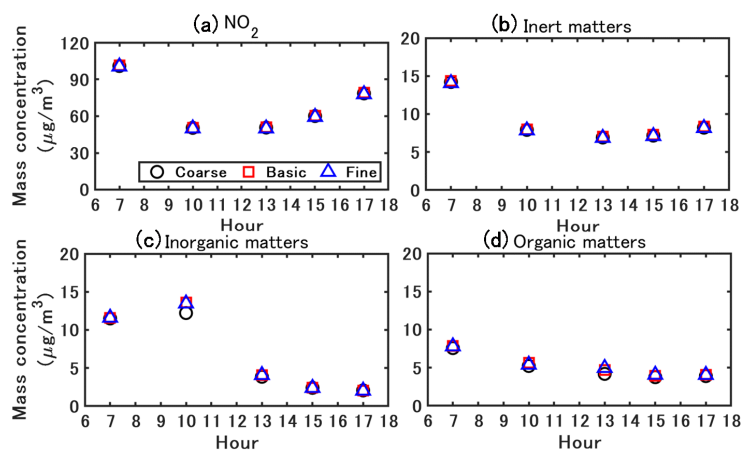
325 Fig. 8 Different grid resolutions for sensitivity analysis: (a) coarse, (b) basic, (c) fine. The
326 grid resolutions in the street canyon are 1 m, 0.5 m and 0.25 m in both x - and z - directions,
327 respectively. The largest grid sizes are 4 m (x) \times 2 m (z) in the coarse and basic grids,
328 and 2 m (x) \times 2 m (z) in the fine grid.

329

330 Grid sensitivity analysis was conducted based on three different resolutions as shown in
331 Fig. 8. The grid resolutions in the street canyon for coarse, basic and fine grids are 1 m,
332 0.5 m and 0.25 m in both x - and z - directions, respectively. The largest grid sizes are 4 m



333 (x) × 2m (z) for the coarse and basic grids, and 2 m (x) × 2m (z) for the fine grid. The
334 simulations were based on constant-condition method. The Strang method, which is
335 introduced in Section 4.4, is used with a time step of 0.5 s. Fig. 9 shows the comparative
336 results for the mass concentration. No significant discrepancy was observed between the
337 different grids for NO₂, inert matters and organic matters. Meanwhile, the simulated
338 inorganic matters based on coarse grids showed slightly smaller concentrations than the
339 other grid resolutions, while the concentrations based on basic and fine grids are close.
340 Therefore, the basic grid was adopted for simulations in this study.



341

342 Fig. 9 Simulated NO₂ and particle concentrations with different grid resolutions.

343

344 4.4. Coupling method and time step sensitivity

345 The transport equation for the chemical species includes terms of advection, diffusion,
346 emission and chemical reactions. Ideally, the transport equation should be solved with all
347 the above terms, that is, by coupling all processes. However, the chemical process is
348 integrated with a stiff integrator, whereas advection, diffusion and emission are integrated
349 with a flux scheme. Therefore, operator splitting (Sportisse, 2000) is often employed to
350 solve different terms individually and sequentially over a given time step in chemical
351 transport simulations (Fu and Liang, 2016).

352 In this study, advection, diffusion and emission were simultaneously solved in CFD, and
353 the chemical reactions including gas chemistry, particle dynamics and size redistribution
354 were solved in SSH-Aerosol. Two integration orders are considered for coupling: a first
355 order method and a Strang method. For the first order method, which can be summarized
356 as CFD(Δt)-Chemistry(Δt), the mass concentrations are first integrated for transport over
357 a time step Δt . The updated concentrations are then integrated for chemistry at the



358 same Δt . This method is first-order accurate in time. To improve accuracy, Strang (1968)
359 introduced a symmetric sequence of operators, which can be summarized as $\text{CFD}(\Delta t/2)$ -
360 $\text{Chemistry}(\Delta t)$ - $\text{CFD}(\Delta t/2)$. The mass concentrations are first integrated for transport over
361 a half time step, then for chemistry over the full time step and finally for transport again
362 over a half time step. The Strang method leads to a second-order accuracy in time.

363

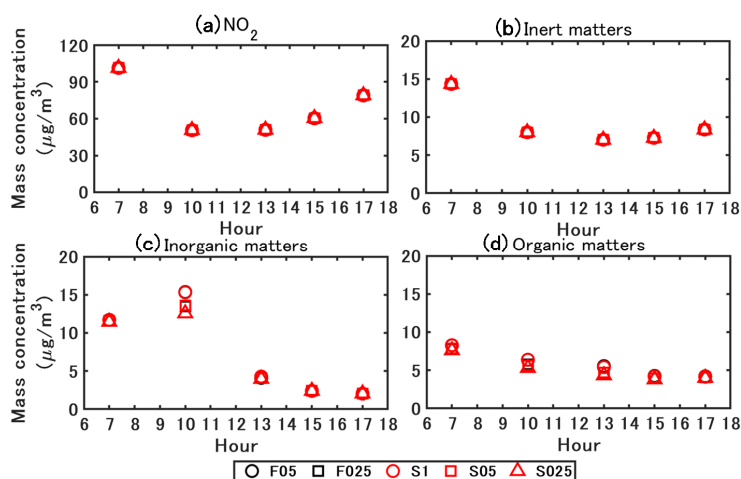
364 Table 2 Relative change in the computation time with different operator-splitting order
365 and time steps. The computation time is normalized by S05.

Case	Operator splitting order	Δt (s)	Change in the computation time
F05	First order method	0.5	0.90
F025	$\text{CFD}(\Delta t)$ - $\text{Chemistry}(\Delta t)$	0.25	1.56
S1	Strang method	1	0.57
S05	$\text{CFD}(\Delta t/2)$ - $\text{Chemistry}(\Delta t)$ - $\text{CFD}(\Delta t/2)$	0.5	1
S025		0.25	2.44

366

367 A sensitivity analysis was conducted on the operator splitting method and splitting time
368 step. As shown in Table 2, the time step is considered 0.5 s and 0.25 s for the first order
369 method (named F05 and F025), and 1 s, 0.5 s and 0.25 s for the Strang method (named
370 S1, S05 and S025). The simulated NO_2 and particle concentrations are presented in Fig.
371 10. S1 and F05 concentrations hardly differed from the figures. Meanwhile, the
372 computational time of S1 was only 63% of that of F05. Similarly, the concentrations
373 simulated with S05 and F025 were almost the same, and the computational time of S05
374 was only 64% of F025. Therefore, the Strang method can be considered as a cost effective
375 method.

376



377

378 Fig. 10 Simulated NO₂ and particle concentrations with different coupling methods and
379 time steps. S denotes the Strang method: CFD($\Delta t/2$)-Chemistry(Δt)-CFD($\Delta t/2$). F
380 denotes the first order method: CFD(Δt)-Chemistry(Δt). In the legend, the values that
381 follow the capital letter S (Strang) or F (First order) denote the time step Δt (in s) used
382 in the simulation.

383

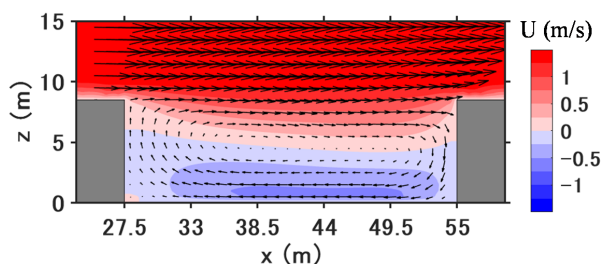
384 The concentrations simulated with the Strang method and different time steps show that
385 small time step results in low inorganic and organic matter concentrations. The
386 concentrations simulated with S1 were larger than those of S05, and larger than S025.
387 However, the differences between the concentrations simulated with S05 and S025 were
388 lower than the differences between S1 and S05. For NO₂ and inert particles, no obvious
389 difference was found between the simulations with different splitting methods and
390 splitting time steps. Therefore, the Strang method with a time step of 0.5 s is adopted in
391 this study.

392



393 **5. Results and discussion**

394 *5.1. Time-averaged flow field and concentration field*

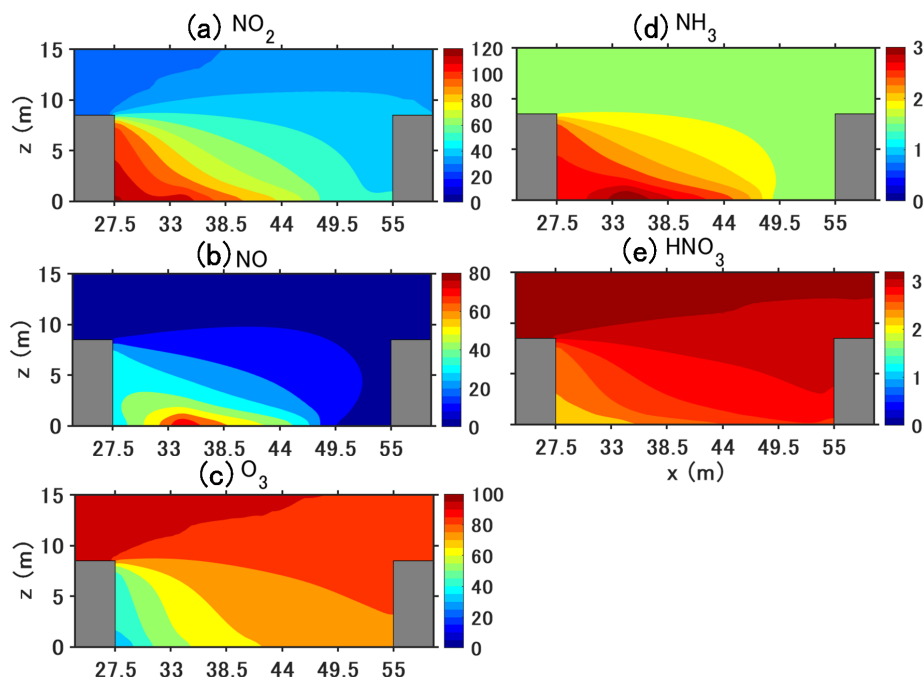


395

396 Fig. 11 Time-averaged flow field in the street canyon from 5 a.m. to 5 p.m.

397

398 This section shows the results for time-averaged values from 5 a.m. to 5 p.m. Fig. 11
399 shows the 12-hour time-averaged streamwise velocity and wind direction in the street
400 canyon. At the current aspect ratio ($H/W=0.31$), a large vortex was observed in the canyon
401 with a small secondary vortex at the corner of the leeward wall. A reverse flow was
402 observed in the lower half of the canyon.



403

404 Fig. 12 Time-averaged concentrations ($\mu\text{g}/\text{m}^3$) of gaseous pollutants in the street canyon

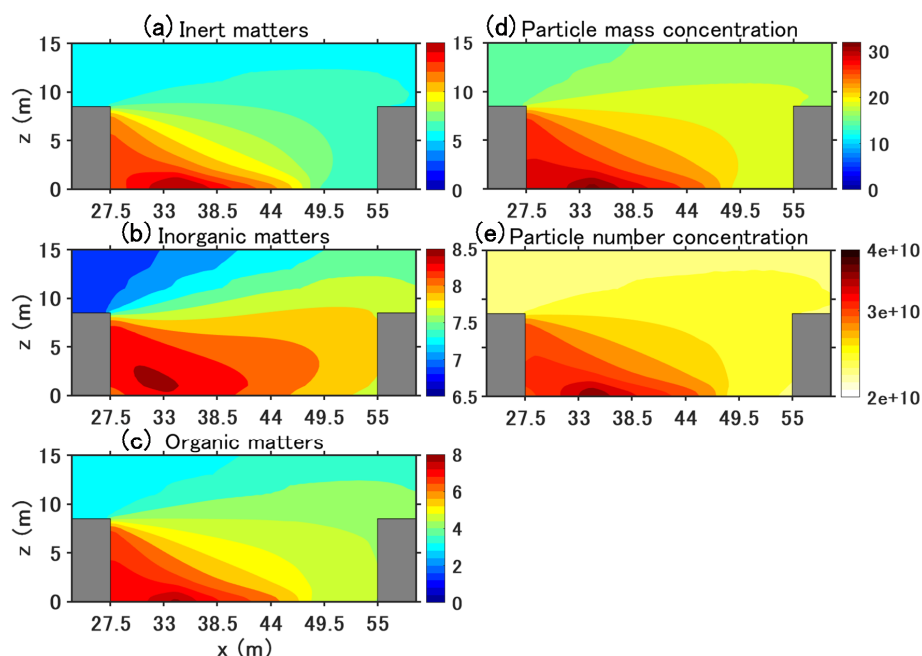


405 from 5 a.m. to 5 p.m.

406

407 Fig. 12 shows the time-averaged concentrations of the gaseous pollutants from 5 a.m. to
408 5 p.m. For gaseous pollutants emitted by traffic, such as NO_2 , NO and NH_3 , larger
409 concentrations are found in the street, particularly near the leeward wall, compared to the
410 windward wall due to the reverse flow. Simultaneously, gas-phase chemistry and
411 condensation/evaporation between the gas and particle phases also influence the
412 concentration distribution. NO_2 mainly increased due to chemical production from NO
413 emissions and background O_3 . Compared to the background NO_2 concentration of 26
414 $\mu\text{g}/\text{m}^3$, the longest retention time at the leeward side corner led to the street canyon's
415 largest concentration ($121 \mu\text{g}/\text{m}^3$). At pedestrian height ($z=1.5 \text{ m}$), NO_2 concentration was
416 $116 \mu\text{g}/\text{m}^3$ at the leeward wall and $49 \mu\text{g}/\text{m}^3$ at the windward wall.

417 However, NO and NH_3 generally decreased because of loss by gaseous chemistry and the
418 condensation of ammonium nitrate, respectively; therefore, the largest concentrations
419 were at the leeward corner of the traffic emission source. For secondary gaseous
420 pollutants without traffic emissions such as O_3 and HNO_3 , gaseous chemistry and
421 condensation led to lower concentrations near the leeward wall than background
422 concentrations. For O_3 , this is due to the titration of O_3 by NO , whose concentration was
423 large near the leeward wall. For HNO_3 , this was because of the high concentrations of
424 NH_3 , which then condensed with HNO_3 to form ammonium nitrate.



425

426 Fig. 13 Time-averaged concentrations of particle number, mass and composition in the
427 street canyon from 5 a.m. to 5 p.m. The unit is $\mu\text{g}/\text{m}^3$ for mass concentration and m^{-3} for
428 number concentration.

429

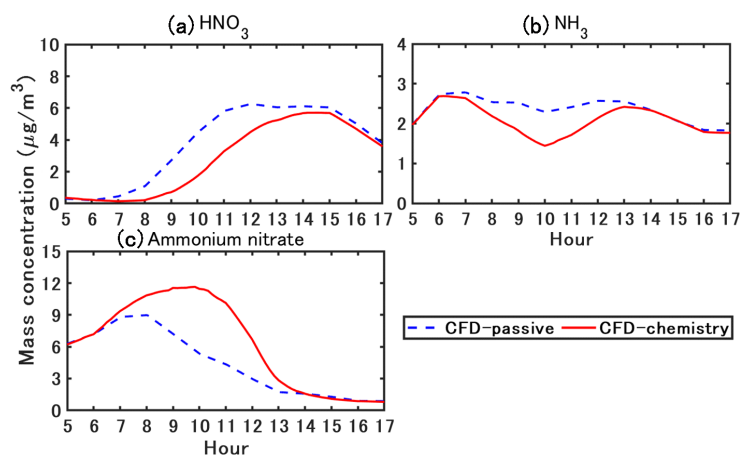
430 Fig. 13 shows the time-averaged PM_{10} mass concentration, and the number
431 concentrations and PM composition (inorganic, organic and inert matters) from 5 a.m. to
432 5 p.m. For inert and organic matters, the highest concentrations were near the leeward
433 corner of the traffic emission source. Because inorganic matters are not emitted, the
434 concentration distribution differs from inert and organic matters. However, as they are
435 produced from gas condensation and strongly influenced by traffic emissions, the highest
436 concentrations were observed in the leeward corner.

437 At pedestrian height ($z=1.5\text{ m}$), the PM_{10} mass concentration was approximately $28\ \mu\text{g}/\text{m}^3$
438 at the leeward wall and $19\ \mu\text{g}/\text{m}^3$ at the windward wall, which is larger than the
439 background concentration of $15\ \mu\text{g}/\text{m}^3$. The number concentration is computed from the
440 mass concentration and therefore has a similar spatial distribution as PM_{10} mass
441 concentration (nucleation from gas was not taken into account). Traffic emission
442 significantly increased the number concentration. The number concentration is about
443 $2.3 \times 10^{10}\ \text{m}^{-3}$ in the background, whereas the largest number concentration in the
444 street canyon is about $3.8 \times 10^{10}\ \text{m}^{-3}$.



445

446 5.2. Time-variant characteristics



447

448 Fig. 14 Simulated time-varying concentrations of ammonium nitrate and precursor gas
449 (HNO_3 and NH_3).

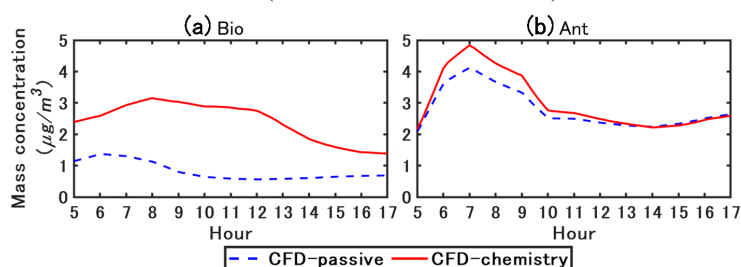
450

451 Fig. 14 shows the simulated time-varying concentrations of ammonium nitrate formed by
452 the condensation of HNO_3 and NH_3 . Based on the traffic fleet in the current study, NH_3
453 emission was approximately 1-2% of NO_x emissions. Ammonium nitrate and HNO_3 are
454 not emitted and differences between simulations with or without chemistry coupling are
455 due to gas chemical reactions and phase change between the gas and particle. Phase
456 change may be driven by NH_3 emissions, as well as the non-thermodynamic equilibrium
457 of the background concentrations.

458 In CFD-passive, NH_3 concentration peaked around 6 am as NO_x because it was emitted
459 by traffic. The peak in HNO_3 concentration was later in the morning, around 11 am. HNO_3
460 is formed from the oxidation of NO_2 , which is emitted by traffic and is rapidly formed
461 from NO traffic emissions. The formation of HNO_3 is slower than the formation of NO_2 ,
462 and probably occurs at the regional scale, leading to a delay in the peak of HNO_3
463 concentration compared to NO_2 concentration. In CFD-chemistry, the temporal variations
464 of HNO_3 concentration show large differences with CFD-passive because HNO_3
465 condenses with NH_3 to form ammonium nitrate during the daytime. As a result, the HNO_3
466 concentration peak in CFD-chemistry was later than that in CFD-passive (it was shifted
467 from 11 a.m. to around 2 p.m.). The NH_3 concentration in CFD-passive peaked at 7 a.m.
468 because of traffic emission and was stable from 7 a.m. to 1 p.m. and then decreased from
469 1 p.m. Meanwhile, the condensation in CFD-chemistry leads to lower concentration than



470 in CFD-passive during the daytime (between 7 a.m. and 1 p.m.).
471 For 12-hour time-averaged concentrations, ammonium nitrate increased by 46% in CFD-
472 chemistry compared with that in CFD-passive. Background ammonium nitrate
473 concentration (CFD-passive) peaked around the morning rush (7 to 8 a.m.) and then
474 decreased. Meanwhile, in CFD-chemistry, ammonium nitrate concentration peaked later
475 around 10 a.m., because of the large increase in HNO_3 between the traffic rush and 10
476 a.m. However, although HNO_3 concentration did not vary much between 11 a.m. and 3
477 p.m., the ammonium nitrate concentration decreased from 10 a.m. to a very small level
478 (lower than $1 \mu\text{g}/\text{m}^3$) after 2 p.m. This decrease is probably linked to the temperature
479 increase during the daytime (Fig. 2(b)) and the relative humidity decrease, leading to a
480 decrease in the condensation rate (Stelson and Seinfeld, 1982).



481
482 Fig. 15 Simulated time-varying concentration of organic matters. Bio refers to organic
483 matter formed from biogenic precursors. Ant refers to organic matter formed from
484 anthropogenic precursors.

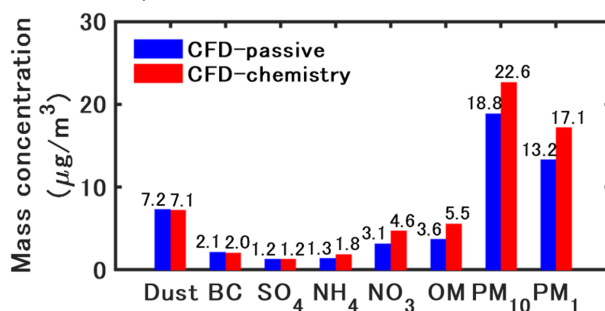
485
486 Fig. 15 shows the simulated time-varying concentrations of organic matters. Organic
487 matters are divided into two main categories depending on the origin of the precursors:
488 Bio and Ant. refer to the organic matter of biogenic and anthropogenic precursors
489 respectively.

490 In CFD-chemistry, Bio concentration is larger than that in CFD-passive. As biogenic
491 precursors are not emitted in the street, the condensation of Bio is due to background
492 precursor gases. As discussed previously, the concentration of ammonium nitrate is higher
493 in CFD-chemistry than in CFD-passive, providing a larger aqueous mass onto which
494 hydrophilic compounds of the biogenic precursor gases condense. As the condensation of
495 ammonium nitrate decreased in the afternoon as shown in Fig. 14, the condensation of
496 Bio also decreased.

497 Ant is largely influenced by traffic emissions in the street, particularly by emissions of
498 semi-volatile compounds (Sartelet et al., 2018), which soon condense after emissions.
499 Therefore there is a peak around 7 a.m. owing to the morning rush. In the model,



500 anthropogenic emissions are mostly hydrophobic, therefore the condensation is not
501 enhanced by the increase in inorganic concentrations. Consequently, the difference
502 between CFD-chemistry and CFD-passive is larger in the morning owing to the large
503 increase in traffic emissions, but small differences are observed in the afternoon.



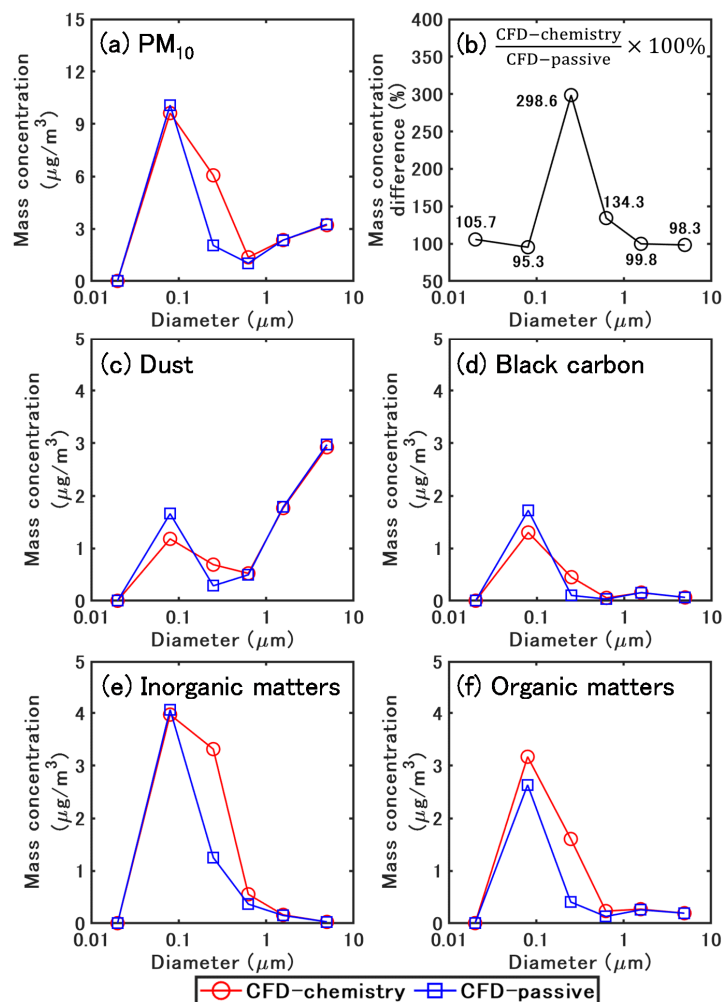
504 Fig. 16 Time-averaged concentration of the chemical compounds of PM₁₀, PM₁₀ and PM₁
505 from 5 a.m. to 5 p.m.
506

507 Fig. 16 shows the time-averaged concentrations of the chemical compounds of PM₁₀,
508 PM₁₀ and PM₁ from 5 a.m. to 5 p.m. The time-averaged PM₁₀ and PM₁ concentrations
509 increased by approximately 3.8 µg/m³ in CFD-chemistry compared to CFD-passive,
510 indicating that chemistry mainly influences small particles. Inert matters slightly decrease
511 in CFD-chemistry owing to dry deposition. Condensation increases of 48%, 38% and
512 53% of nitrate, ammonium and organic matter concentrations in CFD-chemistry
513 compared to CFD-passive.
514

515



516 5.3. Size distribution of particle matters



517
 518 Fig. 17 Time-averaged size distribution of PM_{10} for different chemical species from 5 a.m.
 519 to 5 p.m.

520
 521 Fig. 17 shows the time-averaged size distribution of PM_{10} for the different chemical
 522 compounds of particles from 5 a.m. to 5 p.m. The bound diameters are 0.01, 0.04, 0.16,
 523 0.4, 1.0, 2.5 and 10 μm , and the mean diameters are 0.02, 0.08, 0.25, 0.63, 1.58 and 5.01
 524 μm .

525 For the total concentration of PM_{10} (Fig. 17(a)), the lowest and the largest concentrations
 526 are in the first size section (0.01-0.04 μm) and the second size section (0.04-0.16 μm)



527 respectively, for both the CFD-passive and the CFD-chemistry simulations. Generally,
528 the loss and gain of mass concentration in each size section are related to emission, dry
529 deposition, coagulation (small particles coagulate into large particles), and
530 condensation/evaporation (phase exchange between gas and particles).

531 Fig. 17(b) shows the mass concentration ratio between CFD-passive and CFD-chemistry
532 for each size section. For particles in the size range of 0.04-0.16 μm , the concentrations
533 are smaller in CFD-chemistry than in CFD-passive, because dry deposition and
534 coagulation both decrease mass concentration for those particles. Furthermore, semi-
535 volatile gases may evaporate from small particles because of the Kelvin effect and
536 condense onto larger particles. For particles in the size range of 0.16-1.0 μm , the
537 concentrations are much larger in CFD-chemistry than CFD-passive, indicating that
538 coagulation and condensation on the mass-concentration increase are dominant to other
539 processes, such as deposition. For particles larger than 1 μm , the concentrations of CFD-
540 passive and CFD-chemistry were similar, because particle dynamics have a low influence
541 on large particles.

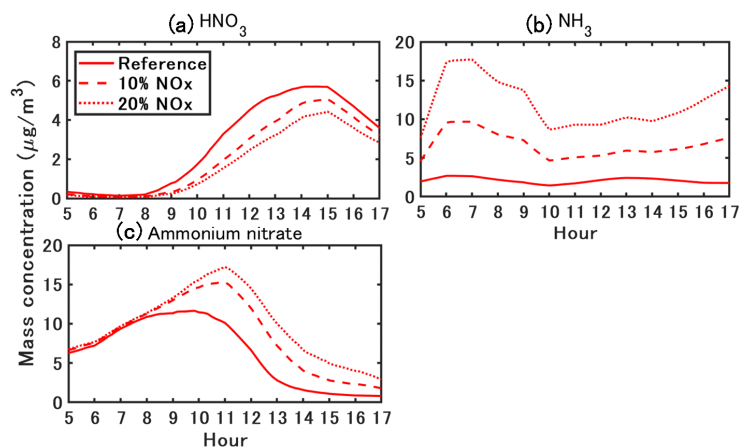
542 The size distribution of dust (Fig. 17(c)) shows that most dust mass concentrations were
543 in particles larger than 1 μm . Meanwhile, most of the mass concentration of BC, inorganic
544 and organic matters (Fig. 17(d-f)) is in particles smaller than 1 μm . Coagulation is the
545 main process influencing the size distribution for inert matters (dust and BC). Compared
546 to CFD-passive, the mass concentration of dust and BC in the second size section
547 decreased by 0.48 and 0.43 $\mu\text{g}/\text{m}^3$ in CFD-chemistry. Correspondingly, the mass
548 concentrations of dust and BC in the third size section increase by 0.41 and 0.35 $\mu\text{g}/\text{m}^3$.
549 For inorganic matters, in the second size section, the concentrations are similar in CFD-
550 passive and CFD-chemistry: particle dynamics decrease sulphate concentration by 0.32
551 $\mu\text{g}/\text{m}^3$ and increase nitrate concentration by 0.17 $\mu\text{g}/\text{m}^3$. However, as the results of the
552 combination effect of coagulation and ammonium nitrate condensation, the
553 concentrations largely increased in the third size section in CFD-chemistry: sulphate,
554 ammonium and nitrate increased by 0.27, 0.6 and 1.24 $\mu\text{g}/\text{m}^3$, respectively.

555 For organic matters, because of condensation of hydrophilic compounds from background
556 biogenic gases and anthropogenic emissions, CFD-chemistry leads to a small increase in
557 concentrations (0.53 $\mu\text{g}/\text{m}^3$) in the second size section and a large increase in the third
558 section (1.21 $\mu\text{g}/\text{m}^3$) compared to CFD-passive. In detail, Bio concentrations increase by
559 0.89 $\mu\text{g}/\text{m}^3$, and Ant concentrations decrease by 0.36 $\mu\text{g}/\text{m}^3$ in the second size section. In
560 the third size section, Bio and Ant concentrations increase by 0.67, 0.54 $\mu\text{g}/\text{m}^3$.

561



562 5.4. Influence of ammonia traffic emissions



563

564 Fig. 18 Sensitivity of NH_3 emission on ammonium nitrate concentration.

565

566 Suarez-Bertoa et al., (2017) conducted on-road measurements of NH_3 emissions from two
567 Euro 6b compliant light duty cars (one gasoline and one diesel) under real-world driving
568 conditions, and they found that NH_3 emissions accounted for 11.9% and 0.92% of NO_x
569 emissions for gasoline and diesel vehicles. As explained in Section 5.2, NH_3 emission
570 emissions were approximately 1-2% of NO_x emissions in the reference case. Two cases
571 were considered to simulate the impact of an increase in the fraction of gasoline cars, and
572 sensitivity simulations were performed with NH_3 emission considered as 10% and 20%
573 of the NO_x emissions.

574 Fig. 18 shows the sensitivity of ammonium nitrate concentration to NH_3 emissions. A
575 larger NH_3 emission delayed the peak of ammonium nitrate by approximately one hour.
576 For a 12-hour average, considering NH_3 emissions of 10% and 20% of NO_x emissions
577 leads to a large increase in ammonium nitrate (35% and 55%) compared to the reference
578 case, because of the formation of ammonium nitrate by the condensation of HNO_3 and
579 NH_3 .

580

581 6. Conclusions

582 Particles in urban environment impose adverse impacts on pedestrians' health.
583 Conventional CFD methods regarding particles as passive scalars cannot reproduce the
584 formation of secondary aerosols and may lead to uncertain simulations. Therefore, to
585 increase the simulation accuracy of particle dispersion, we coupled the CFD software
586 OpenFOAM (OF) and Code_Saturne (CS) with SSH-Aerosol, a modular box model to



587 simulate the evolution of primary and secondary aerosols. The main processes involved
588 in the aerosol dynamics (coagulation, condensation /evaporation and dry deposition) were
589 considered.

590 We simulated a 12-hour transient dispersion of pollutants from traffic emissions in a street
591 canyon using the unsteady RANS model. The simulation domain and background
592 concentration were based on field measurements. The flow field is based on the WRF
593 model. The particle diameter range (0.01 μm to 10 μm) was divided into six size sections.
594 The following conclusions were drawn from the results of this study.

595 1) The simulated spatially-averaged values in the street canyon were validated from
596 field measurement using validation metrics. For both OF and CS, the simulated NO_2
597 and PM_{10} concentrations based on the coupling model (CFD-chemistry) achieved
598 better agreement with the measurement data than the conventional CFD simulation
599 which considers pollutants as passive scalars (CFD-passive). The differences
600 between of the OF and CS results are not obvious and are mainly due to the
601 differences in the turbulence scheme. The following conclusions were drawn based
602 on the simulated OF concentrations.

603 2) For the flow field, a large vortex was observed in the canyon with a small secondary
604 vortex at the corner of the leeward wall at the current aspect ratio ($H/W=0.31$). In
605 CFD-chemistry, because of the reverse flow, the 12-hour (from 5 a.m. to 5 p.m.) time-
606 averaged NO_2 mass concentration, PM_{10} mass and number concentrations at
607 pedestrian height were much higher near the leeward wall ($116 \mu\text{g}/\text{m}^3$, $28 \mu\text{g}/\text{m}^3$,
608 $3.2 \times 10^{10} \text{m}^{-3}$) than the background ($26 \mu\text{g}/\text{m}^3$, $15 \mu\text{g}/\text{m}^3$, $2.3 \times 10^{10} \text{m}^{-3}$).

609 3) Secondary aerosol formation largely affects the mass concentration and size
610 distribution of particle matters. For 12-hour time-averaged concentrations,
611 ammonium nitrate and organic matters increased by 46% and 53% in CFD-chemistry
612 compared to CFD-passive because of condensation of HNO_3 and NH_3 , background
613 biogenic precursor-gases and anthropogenic precursor-gas emissions. Coagulation
614 largely influenced the size distribution of small particles by combining particles with
615 a diameter of 0.04-0.16 μm into 0.16-0.4 μm . At the same time, CFD-chemistry
616 showed a much larger concentration than CFD-passive for the particles in 0.16-1.0
617 μm , indicating that the effect of condensation on increasing mass concentration was
618 dominant compared to other chemical processes.

619 4) Urban areas are NH_3 -limited (HNO_3 sufficient) areas, therefore, increasing NH_3 leads
620 to a large increase in ammonium nitrate. Vehicles are considered to be the main
621 source of NH_3 in urban environments. Increasing the fleet's proportion of recent
622 gasoline vehicles may increase NH_3 emissions. For a 12-hour average, we considered



623 NH₃ emissions of 10% and 20% of NO_x emissions led to a large increase in
624 ammonium nitrate (35% and 55%) compared to the reference case which considers
625 NH₃ emission as 1-2% of NO_x emissions.

626 5) A grid sensitivity analysis showed that the particles' concentrations of inorganic and
627 organic compounds were sensitive to grid resolution, whereas inert particle
628 concentrations were not sensitive to grid resolution. In addition, simulated values
629 based on a grid size of 0.5 m in the street canyon showed small differences with a
630 grid size of 0.25 m, indicating that a spatial resolution of 0.5 m can be enough for
631 reactive particle dispersion at the street level.

632 6) Operator splitting is often employed to solve the transport term and chemical
633 reactions over a given time step in chemical transport simulations. Two integration
634 orders were considered: first order method (CFD(Δt)-Chemistry(Δt)) and Strang
635 method (CFD($\Delta t/2$)-Chemistry(Δt)-CFD($\Delta t/2$)). The results showed that the Strang
636 method had almost the same concentrations as the first order method with half the
637 computational time. Further sensitivity analysis on the time step showed that a time
638 step of 0.5 s was enough when using the Strang method.

639 7) Conducting a CFD simulation with constant boundary conditions and emission rates
640 at a specific time point is considered a practical method to achieve time-averaged
641 concentrations for evaluating street-level pollutant concentrations. The validation
642 was conducted using conditions on five time points (7 a.m., 10 a.m., 1 p.m., 3 p.m.
643 and 5 p.m.). The simulated concentration based on the above method exhibited
644 almost the same value as the simulation with transient conditions at the same time
645 points.

646 Future work will be conducted on the influence of environmental factors and emission
647 conditions, aiming to provide knowledge to devise suitable countermeasures to decrease
648 particle concentration in microscale urban environments.

649

650 Acknowledgments: This work benefited from discussions with Bertrand Carissimo. The
651 authors acknowledge funding from DIM QI² (Air Quality Research Network on air
652 quality in the Île-de-France region) and from Île-de-France region.

653

654 Code/Data availability

655 The codes used in this publication are available to the community, and they can be
656 accessed by request to the corresponding author.

657

658 Author contribution



659 KS and RO were responsible for conceptualization. CL, YW, CF, YK and ZW developed
660 the software. CL and YW conducted the visualization and validation; CL, YW and KS
661 performed the formal analysis. KS, YK and RO acquired resources. CL, YW, RO and KS
662 were responsible for writing and original draft preparation. CF, YK, HK reviewed and
663 edited the manuscript All co-authors contributed to the discussion of the paper.

664

665 Competing interests

666 The contact author has declared that neither they nor their co-authors have any
667 competing interests.

668

669 Reference

670 Anenberg, S. C., Miller, J., Minjares, R., Du, L., Henze, D. K., Lacey, F., Malley, C. S.,
671 Emberson, L., Franco, V., Klimont, Z. and Heyes, C.: Impacts and mitigation of excess
672 diesel-related NO_x emissions in 11 major vehicle markets, *Nature*, 545(7655), 467–
673 471, doi:10.1038/nature22086, 2017.

674 Anon: EMEP/EEA: EMEP/EEA air pollutant emission inventory guidebook 2019, EEA
675 Report No 13/2019, European Environment Agency, [online] Available from:
676 <https://www.eea.europa.eu/publications/emep-eea-guidebook-2019> (Accessed 14 March
677 2022), n.d.

678 Archambeau, F., Méchitoua, N. and Sakiz, M.: Code Saturne: A Finite Volume Code
679 for Turbulent flows - Industrial Applications, *Int. J. Finite Vol.*, 1(1) [online] Available
680 from: <http://www.latp.univ-mrs.fr/IJFV/spip.php?article3&hal-01115371>, 2004.

681 Arpaci, V. S. and Larsen, P. S.: *Convection Heat Transfer*, Prentice Hall, New York.,
682 1984.

683 Belcher, S. E.: Mixing and transport in urban areas, *Philos. Trans. R. Soc. A Math.*
684 *Phys. Eng. Sci.*, 363(1837), 2947–2968, doi:10.1098/rsta.2005.1673, 2005.

685 Bishop, G. A. and Stedman, D. H.: Reactive Nitrogen Species Emission Trends in Three
686 Light-/Medium-Duty United States Fleets, *Environ. Sci. Technol.*, 49(18), 11234–
687 11240, doi:10.1021/acs.est.5b02392, 2015.

688 Blocken, B., Tominaga, Y. and Stathopoulos, T.: CFD simulation of micro-scale
689 pollutant dispersion in the built environment, *Build. Environ.*, 64, 225–230,
690 doi:10.1016/j.buildenv.2013.01.001, 2013.

691 Chang, J. C. and Hanna, S. R.: Air quality model performance evaluation, *Meteorol.*
692 *Atmos. Phys.*, 87(1–3), 167–196, doi:10.1007/s00703-003-0070-7, 2004.

693 Du, Y., Xu, X., Chu, M., Guo, Y. and Wang, J.: Air particulate matter and
694 cardiovascular disease: The epidemiological, biomedical and clinical evidence, *J.*



- 695 Thorac. Dis., 8(1), E8–E19, doi:10.3978/j.issn.2072-1439.2015.11.37, 2016.
- 696 Ferrero, E., Alessandrini, S., Anderson, B., Tomasi, E., Jimenez, P. and Meech, S.:
697 Lagrangian simulation of smoke plume from fire and validation using ground-based
698 lidar and aircraft measurements, *Atmos. Environ.*, 213, 659–674,
699 doi:10.1016/j.atmosenv.2019.06.049, 2019.
- 700 Fu, K. and Liang, D.: The conservative characteristic FD methods for atmospheric
701 aerosol transport problems, *J. Comput. Phys.*, 305, 494–520,
702 doi:10.1016/j.jcp.2015.10.049, 2016.
- 703 Gao, S., Kurppa, M., Chan, C. K. and Ngan, K.: Technical note: Dispersion of cooking-
704 generated aerosols from an urban street canyon, *Atmos. Chem. Phys.*, 22(4), 2703–
705 2726, doi:10.5194/acp-22-2703-2022, 2022.
- 706 Guimet, V. and Laurence, D.: A linearised turbulent production in the k- ϵ model for
707 engineering applications, in *Engineering Turbulence Modelling and Experiments 5*,
708 edited by W. Rodi and N. Fueyo, pp. 157–166, Elsevier Science Ltd, Oxford, UK.,
709 2002.
- 710 Hanna, S. R., Hansen, O. R. and Dharmavaram, S.: FLACS CFD air quality model
711 performance evaluation with Kit Fox, MUST, Prairie Grass, and EMU observations,
712 *Atmos. Environ.*, 38(28), 4675–4687, doi:10.1016/j.atmosenv.2004.05.041, 2004.
- 713 Harten, A.: On a Class of High Resolution Total-Variation-Stable Finite-Difference
714 Schemes, *SIAM J. Numer. Anal.*, 21(1), 1–23, doi:10.1137/0721001, 1984.
- 715 Jones, A. M., Yin, J. and Harrison, R. M.: The weekday–weekend difference and the
716 estimation of the non-vehicle contributions to the urban increment of airborne
717 particulate matter, *Atmos. Environ.*, 42(19), 4467–4479,
718 doi:10.1016/j.atmosenv.2008.02.001, 2008.
- 719 Kim, M. J.: Sensitivity of nitrate aerosol production to vehicular emissions in an urban
720 street, *Atmosphere (Basel)*, 10(4), 212, doi:10.3390/ATMOS10040212, 2019.
- 721 Kim, M. J., Park, R. J., Kim, J. J., Park, S. H., Chang, L. S., Lee, D. G. and Choi, J. Y.:
722 Computational fluid dynamics simulation of reactive fine particulate matter in a street
723 canyon, *Atmos. Environ.*, 209, 54–66, doi:10.1016/j.atmosenv.2019.04.013, 2019.
- 724 Kim, Y., Wu, Y., Seigneur, C. and Roustan, Y.: Multi-scale modeling of urban air
725 pollution: development and application of a Street-in-Grid model (v1.0) by coupling
726 MUNICH (v1.0) and Polair3D (v1.8.1), *Geosci. Model Dev.*, 11(2), 611–629,
727 doi:10.5194/gmd-11-611-2018, 2018.
- 728 Kim, Y., Lugon, L., Maison, A., Sarica, T., Roustan, Y., Valari, M., Zhang, Y., André,
729 M., Sartelet, K., Paris-saclay, U. and Ecosys, U. M. R.: MUNICH v2.0: A street-
730 network model coupled with SSH-aerosol (v1.2) for multi-pollutant modelling, *Geosci.*



- 731 Model Dev., submitting.
- 732 Kumar, P., Fennell, P., Langley, D. and Britter, R.: Pseudo-simultaneous measurements
733 for the vertical variation of coarse, fine and ultrafine particles in an urban street canyon,
734 Atmos. Environ., 42(18), 4304–4319, doi:10.1016/j.atmosenv.2008.01.010, 2008.
- 735 Kurppa, M., Hellsten, A., Roldin, P., Kokkola, H., Tonttila, J., Auvinen, M., Kent, C.,
736 Kumar, P., Maronga, B. and Järvi, L.: Implementation of the sectional aerosol module
737 SALSAA2.0 into the PALM model system 6.0: Model development and first evaluation,
738 Geosci. Model Dev., 12(4), 1403–1422, doi:10.5194/gmd-12-1403-2019, 2019.
- 739 Lo, K. W. and Ngan, K.: Characterising the pollutant ventilation characteristics of street
740 canyons using the tracer age and age spectrum, Atmos. Environ., 122, 611–621,
741 doi:10.1016/j.atmosenv.2015.10.023, 2015.
- 742 Lo, K. W. and Ngan, K.: Characterizing ventilation and exposure in street canyons
743 using Lagrangian particles, J. Appl. Meteorol. Climatol., 56(5), 1177–1194,
744 doi:10.1175/JAMC-D-16-0168.1, 2017.
- 745 Lugon, L., Vigneron, J., Debert, C., Chrétien, O. and Sartelet, K.: Black carbon
746 modeling in urban areas: investigating the influence of resuspension and non-exhaust
747 emissions in streets using the Street-in-Grid model for inert particles (SinG-inert),
748 Geosci. Model Dev., 14(11), 7001–7019, doi:10.5194/gmd-14-7001-2021, 2021a.
- 749 Lugon, L., Sartelet, K., Kim, Y., Vigneron, J. and Chretien, O.: Simulation of primary
750 and secondary particles in the streets of Paris using MUNICH, Faraday Discuss.,
751 226(0), 432–456, doi:10.1039/d0fd00092b, 2021b.
- 752 OpenFOAM: OpenFOAM user guide, [online] Available from:
753 <https://www.openfoam.com/>, 2020.
- 754 Parente, A., Gorié, C., van Beeck, J. and Benocci, C.: Improved $k-\epsilon$ model and wall
755 function formulation for the RANS simulation of ABL flows, J. Wind Eng. Ind.
756 Aerodyn., 99(4), 267–278, doi:10.1016/j.jweia.2010.12.017, 2011.
- 757 Di Sabatino, S., Buccolieri, R., Pulvirenti, B. and Britter, R.: Simulations of pollutant
758 dispersion within idealised urban-type geometries with CFD and integral models,
759 Atmos. Environ., 41(37), 8316–8329, doi:10.1016/j.atmosenv.2007.06.052, 2007.
- 760 Sartelet, K., Zhu, S., Moukhtar, S., André, M., André, J. M., Gros, V., Favez, O.,
761 Brasseur, A. and Redaelli, M.: Emission of intermediate, semi and low volatile organic
762 compounds from traffic and their impact on secondary organic aerosol concentrations
763 over Greater Paris, Atmos. Environ., 180, 126–137,
764 doi:10.1016/j.atmosenv.2018.02.031, 2018.
- 765 Sartelet, K., Couvidat, F., Wang, Z., Flageul, C. and Kim, Y.: SSH-aerosol v1.1: A
766 modular box model to simulate the evolution of primary and secondary aerosols,



- 767 Atmosphere (Basel), 11(5), 525, doi:10.3390/atmos11050525, 2020.
- 768 Sartelet, K. N., Debry, E., Fahey, K., Roustan, Y., Tombette, M. and Sportisse, B.:
769 Simulation of aerosols and gas-phase species over Europe with the Polyphemus system:
770 Part I-Model-to-data comparison for 2001, Atmos. Environ., 41(29), 6116–6131,
771 doi:10.1016/j.atmosenv.2007.04.024, 2007.
- 772 Sportisse, B.: An Analysis of Operator Splitting Techniques in the Stiff Case, J.
773 Comput. Phys., 161(1), 140–168, doi:10.1006/jcph.2000.6495, 2000.
- 774 Stelson, A. W. and Seinfeld, J. H.: Relative humidity and temperature dependence of
775 the ammonium nitrate dissociation constant, Atmos. Environ., 16(5), 983–992,
776 doi:10.1016/0004-6981(82)90184-6, 1982.
- 777 Strang, G.: On the Construction and Comparison of Difference Schemes, SIAM J.
778 Numer. Anal., 5(3), 506–517, doi:10.1137/0705041, 1968.
- 779 Suarez-Bertoa, R. and Astorga, C.: Impact of cold temperature on Euro 6 passenger car
780 emissions, Environ. Pollut., 234, 318–329, doi:10.1016/j.envpol.2017.10.096, 2018.
- 781 Suarez-Bertoa, R., Mendoza-Villafuerte, P., Riccobono, F., Vojtisek, M., Pechout, M.,
782 Perujo, A. and Astorga, C.: On-road measurement of NH₃ emissions from gasoline and
783 diesel passenger cars during real world driving conditions, Atmos. Environ., 166, 488–
784 497, doi:10.1016/j.atmosenv.2017.07.056, 2017.
- 785 Sun, K., Tao, L., Miller, D. J., Pan, D., Golston, L. M., Zondlo, M. A., Griffin, R. J.,
786 Wallace, H. W., Leong, Y. J., Yang, M. M., Zhang, Y., Mauzerall, D. L. and Zhu, T.:
787 Vehicle Emissions as an Important Urban Ammonia Source in the United States and
788 China, Environ. Sci. Technol., 51(4), 2472–2481, doi:10.1021/acs.est.6b02805, 2017.
- 789 Sung, J. C., Pulliam, B. L. and Edwards, D. A.: Nanoparticles for drug delivery to the
790 lungs, Trends Biotechnol., 25(12), 563–570, doi:10.1016/j.tibtech.2007.09.005, 2007.
- 791 Tominaga, Y. and Stathopoulos, T.: Turbulent Schmidt numbers for CFD analysis with
792 various types of flowfield, Atmos. Environ., 41(37), 8091–8099,
793 doi:10.1016/j.atmosenv.2007.06.054, 2007.
- 794 Tominaga, Y. and Stathopoulos, T.: CFD simulation of near-field pollutant dispersion in
795 the urban environment: A review of current modeling techniques, Atmos. Environ., 79,
796 716–730, doi:10.1016/j.atmosenv.2013.07.028, 2013.
- 797 Trini Castelli, S., Armand, P., Tinarelli, G., Duchenne, C. and Nibart, M.: Validation of
798 a Lagrangian particle dispersion model with wind tunnel and field experiments in urban
799 environment, Atmos. Environ., 193, 273–289, doi:10.1016/j.atmosenv.2018.08.045,
800 2018.
- 801 Wesely, M. L.: Parameterization of surface resistances to gaseous dry deposition in
802 regional-scale numerical models, Atmos. Environ., 23(6), 1293–1304,



- 803 doi:10.1016/0004-6981(89)90153-4, 1989.
- 804 Wu, L., Hang, J., Wang, X., Shao, M. and Gong, C.: APFoam 1.0: Integrated
805 computational fluid dynamics simulation of O₃-NO_x-volatile organic compound
806 chemistry and pollutant dispersion in a typical street canyon, *Geosci. Model Dev.*,
807 14(7), 4655–4681, doi:10.5194/gmd-14-4655-2021, 2021.
- 808 Yakhot, V., Orszag, S. A., Thangam, S., Gatski, T. B. and Speziale, C. G.: Development
809 of turbulence models for shear flows by a double expansion technique, *Phys. Fluids A*,
810 4(7), 1510–1520, doi:10.1063/1.858424, 1992.
- 811 Yee, H. C.: Construction of explicit and implicit symmetric TVD schemes and their
812 applications, *J. Comput. Phys.*, 68(1), 151–179, doi:10.1016/0021-9991(87)90049-0,
813 1987.
- 814 Zhang, K., Chen, G., Zhang, Y., Liu, S., Wang, X., Wang, B. and Hang, J.: Integrated
815 impacts of turbulent mixing and NO_x-O₃ photochemistry on reactive pollutant
816 dispersion and intake fraction in shallow and deep street canyons, *Sci. Total Environ.*,
817 712, 135553, doi:10.1016/j.scitotenv.2019.135553, 2020.
- 818 Zhang, L., Gong, S., Padro, J. and Barrie, L.: A size-segregated particle dry deposition
819 scheme for an atmospheric aerosol module, *Atmos. Environ.*, 35(3), 549–560,
820 doi:10.1016/S1352-2310(00)00326-5, 2001.
- 821 Zhang, L., Brook, J. R. and Vet, R.: A revised parameterization for gaseous dry
822 deposition in air-quality models, *Atmos. Chem. Phys.*, 3(6), 2067–2082,
823 doi:10.5194/acp-3-2067-2003, 2003.

824

825 Appendix A

826 The schemes for particle deposition velocity v_d were added to the transport equations
827 using volume sink terms based on Zhang et al. (2001) and can be represented as:

$$v_{d,p} = \begin{cases} v_g + \frac{1}{R_a + R_s}, & \text{Wall surfaces} \\ v_g, & \text{Entire field} \end{cases} \quad (\text{A1})$$

$$v_g = \frac{\rho d_p^2 g C}{18\eta} \quad (\text{A2})$$

$$R_a = \frac{\ln(z_R/z_0) - \psi_H}{\kappa u_*} \quad (\text{A3})$$

$$R_s = \frac{1}{\varepsilon_0 u_* (E_B + E_{IM} + E_{IN}) R_1} \quad (\text{A4})$$



828 The deposition velocity for the particles $v_{d,p}$ consists of both gravitational settling and
829 surface deposition near the wall surfaces. The gravitational settling velocity v_g was
830 considered for the entire field, ρ is the particle density; d_p is the particle diameter; g
831 is the acceleration of gravity; C is Cunningham correction factor for small particles; η
832 is the viscosity coefficient of air.

833 The aerodynamic resistance R_a is calculated from the first-layer-height z_R , roughness
834 length z_0 , Von Karman constant κ , friction velocity u_* and stability function ψ_H . For the
835 k- ϵ model, u_* is estimated by $(C_\mu^{0.5}k)^{0.5}$ and $C_\mu = 0.09$ is a constant of the model.

836 The surface resistance R_s is calculated from u_* , the collection efficiency from Brownian
837 diffusion E_B , the impaction E_{IM} and the interception E_{IN} . The correction factor
838 represents the fraction of particles that stick to the surface R_1 and an empirical
839 constant $\epsilon_0 = 3$.

840 The dry deposition schemes for gas were added to the transport equations using volume
841 sink terms based on Wesely (1989) and Zhang et al. (2003), which can be represented as:

$$v_{d,g} = \frac{1}{R_a + R_b + R_c} \quad (\text{A1})$$

$$R_b = \frac{2}{\kappa u_*} \left(\frac{Sc}{Pr} \right)^{2/3} \quad (\text{A2})$$

842 The deposition velocity for gas $v_{d,g}$ is calculated from the aerodynamic resistance R_a ,
843 the quasi-laminar layer resistance R_b and the surface resistance for gas R_c . $Sc = \nu/D$
844 and $Pr = 0.72$ are the Schmidt and Prandtl number. ν is the kinematic viscosity of air
845 and D is the molecular diffusivity of different gases. R_c is calculated based on Zhang
846 et al. (2003).